Materials Advances

ROYAL SOCIETY OF CHEMISTRY

PAPER

View Article Online
View Journal | View Issue

Check for updates

Cite this: *Mater. Adv.*, 2025, 6, 2521

A carbazole-based fully conjugated sp^2c D–A covalent organic polymer for visible light mediated photocatalytic degradation of rhodamine B and Rose Bengal†

Kamal Verma and K. R. Justin Thomas *

Two-dimensional covalent organic materials have great potential as photocatalysts, but for practical application, they have some limitations like scalability and stability. Nevertheless, ongoing research efforts aim to address these challenges and unlock their full potential for sustainable photocatalysis. In this study, we have developed sp^2 carbon-linked and imine-linked 2D donor–acceptor CzTA-PDAN and CzTA-PDA COPs. Notably, the sp^2 carbon-linked CzTA-PDAN COP demonstrates superior charge separation, rapid photocurrent response, and excellent chemical stability compared to the imine-linked CzTA-PDA COP, owing to its fully conjugated robust structure. The band gap calculated from the Kubelka–Munk plot was 2.30 eV and 2.53 eV, respectively, which resulted in the sp^2c CzTA-PDAN COP having a higher electron carrier transport efficiency. Leveraging its favorable photo and optoelectronic properties, we employed the CzTA-PDAN COP for the photocatalytic degradation of organic toxic dyes, rhodamine B and Rose Bengal, under 18 W white CFL illumination for 80 minutes and 390 minutes, respectively. Additionally, the sp^2 carbon-linked CzTA-PDAN COP exhibited exceptional degradation performance even under sunlight, achieving complete degradation of the RhB dye within 60 minutes of irradiation. This highlights the practical applicability and versatility of the CzTA-PDAN COP in environmental remediation scenarios. By harnessing the unique properties of COPs, such as those demonstrated by the sp^2 carbon-linked CzTA-PDAN COP, we can pave the way for their widespread adoption in sustainable photocatalysis applications.

Received 26th November 2024,
Accepted 26th February 2025

DOI: 10.1039/d4ma01164c

rsc.li/materials-advances

Open Access Article. Published on 11 March 2025. Downloaded on 2/9/2026 11:40:02 PM.
This article is licensed under a Creative Commons Attribution-NonCommercial 3.0 Unported Licence.

Introduction

Water is the most essential component of the Earth for sustaining life and facilitating various ecological processes.[1] The discharge of dye waste from industries contaminates water, leading to harmful effects on aquatic ecosystems and endangering marine life.[2] Among the diverse categories of dyes, xanthene dyes enjoy widespread usage.[3] These dyes are identified by the presence of a xanthene nucleus containing aromatic groups, defining their chromophoric properties. Rhodamine B[4] (RhB) and Rose Bengal[5] (RB) belong to the group of xanthene dyes, utilized within the textile industry for coloring purposes,[6–8] in photochemical industries for organic transformation,[9–13] and in biology for its fluorescence staining properties.[14–17] It has been observed that the extensive utilization of these dyes presents significant hazards to both human health and the environment,[18] especially when exposure occurs over prolonged periods or at elevated concentrations. Consequently, researchers are increasingly focused on developing strategies for the removal of these dyes from wastewater to address these pressing concerns. Conventional treatment techniques such as centrifugation, sedimentation, flocculation, and biological treatment have limitations, including low removal efficiency and the need for complex equipment.[19] In recent years, photocatalytic degradation of organic dyes become a promising strategy for the treatment of industrial wastewater.[20] Developing appropriate photocatalysts to meet practical requirements poses a significant challenge for this environmentally friendly approach, particularly in the case of photocatalysts capable of harnessing abundant solar energy directly. In the past, there has been a reliance on inorganic semiconductors, particularly metal oxides, for photocatalysis.[21–25] However, these choices come with drawbacks. Metal-containing semiconductors not only introduce harmful metals into the environment but also exhibit instability when exposed to harsh conditions. To overcome the disadvantages of inorganic photocatalysts, covalent porous organic polymers have been investigated for the generation of ROS (reactive

Organic Materials Laboratory, Department of Chemistry, Indian Institute of Technology Roorkee, Roorkee – 247667, India. E-mail: krjt@cy.iitr.ac.in

† Electronic supplementary information (ESI) available. See DOI: https://doi.org/10.1039/d4ma01164c

© 2025 The Author(s). Published by the Royal Society of Chemistry

Open Access Article. Published on 11 March 2025. Downloaded on 2/9/2026 11:40:02 PM.
This article is licensed under a Creative Commons Attribution-NonCommercial 3.0 Unported Licence.

oxygen species).[26] The reported porous polymer photocatalysts include covalent triazine frameworks,[27–30] conjugated microporous polymers,[31–34] and porous aromatic frameworks.[35] Remarkably, researchers not only developed numerous porous organic polymers but have also tailored their topologies and morphological characteristics to effectively tackle the challenge of organic dye photodegradation. Covalent organic polymers[36] (COPs) have advantages such as excellent charge carrier mobility,[37,38] large surface area,[39,40] tunable pore size,[41] low density,[42] high thermal stability, and controllable structural features.[43] Due to all these properties, covalent organic polymers (COPs) find application in gas sorption,[44] sensing,[45,46] optoelectronics,[47] and photocatalysis.[48–52] In general, the photocatalytic activity of the organic photocatalyst is limited to the separation kinetics; therefore, the introduction of a donor–acceptor motif in the polymer framework inhibited the recombination of charge carriers, thereby improving the photocatalytic efficiency of the COP materials. Because of extended conjugation, D–A COPs possess high charge separation efficiency and a wide absorption range in the visible region. All these properties of the D–A COPs make them an ideal candidate for heterogeneous photocatalysis. Carbon–carbon linked COPs possess outstanding chemical stability and uninterrupted π-conjugation as compared to imine-linked COPs due to strong covalent bonding between the building molecules.[53–58] Moreover, the incorporation of heteroaromatic rigid carbazole and triazine building units not only enhances the stability of the framework under harsh conditions but also improves the charge separation and transportation properties of the framework.[59] Previously carbazole-based building blocks have been utilized to fabricate different COPs for photocatalysis and have been showing remarkable performance.[60,61] So, in this way synthesis of carbazole-based COPs as photocatalysts is highly meaningful, as they would perform well in the photocatalytic degradation of organic pollutants. Herein, we have synthesized carbazole and triazine containing sp^2 hybridized C–C and imine linked D–A CzTA-PDAN and CzTA-PDA COPs by a solvothermal method. Due to its good charge separation and transportation properties, the CzTA-PDAN COP was found to be effective for photocatalytic degradation of rhodamine B and Rose Bengal under the irradiation of visible light as well as sunlight. As expected, the sp^2 carbon-linked COP shows impressive efficiency for the degradation of both organic dyes with excellent long-term stability. This study presents a novel approach to enhancing the photocatalytic performance by comparing sp^2 carbon-linked (CzTA-PDAN) and imine-linked (CzTA-PDA) covalent organic frameworks (COFs). The sp^2 carbon-linked CzTA-PDAN COF exhibits superior charge separation, electron transport efficiency, and photocurrent response, with a lower band gap (2.30 eV) compared to the imine-linked counterpart (2.53 eV). Utilizing these properties, CzTA-PDAN demonstrates remarkable photocatalytic degradation of organic dyes, achieving complete degradation within 60 minutes under sunlight underscoring the real-world applicability in environmental remediation. This work addresses traditional limitations of COPs, such as stability, paving the way for their widespread adoption in sustainable photocatalysis applications.

Results and discussion

Synthesis of the CzTA-PDAN COP

We selected 4,4′,4″-(9*H*-carbazole-3,6,9-triyl)tribenzaldehyde (CzTA) as a node and 1,4-phenyldiacetonitrile (PDAN) as a linker to synthesize a new COP having an olefin linkage (Fig. 1a). The olefin-linked CzTA-PDAN COP was synthesized by the Knoevenagel condensation reaction between CzTA and PDAN monomers in the presence of 4 M KOH at 120 °C for 72 h using the solvent system dioxane/mesitylene (*v*/*v* 4/1) (Fig. 1; for detailed information see the ESI,† Scheme S2).

Structural analysis

The chemical structures of both COPs were confirmed by Fourier transform infrared (FT-IR) and ^{13}C cross-polarization/magic angle spinning solid-state nuclear magnetic resonance (CP/MAS ssNMR) spectroscopy. In FT-IR, the CzTA-PDAN COP (Fig. 1b) exhibited a reduction in the intensity of the carbonyl peak at 1698 cm^{-1} and a noticeable shift of the cyano group from 2252 cm^{-1} to 2215 cm^{-1}. Similarly, the CzTA-PDA COP displayed a distinct signal at 1623 cm^{-1}, indicative of the formation of an imine linkage, accompanied by the attenuation of the carbonyl peak (Fig. S2, ESI†), thereby providing evidence for the transformation of the monomer into a polymer structure. In the ^{13}C CP/MAS ssNMR spectrum of the CzTA-PDAN COP, the signals appearing around 108 ppm and 119 ppm correspond to the carbon atom linked to the cyano group and the carbon within the cyano group (Fig. 1c), respectively.

The crystalline structure of two carbazole-based COPs was confirmed by powder X-ray diffraction (PXRD) analysis, and the PXRD pattern of CzTA-PDAN (Fig. 1d) and CzTA-PDA COPs reveals the amorphous nature of the materials (Fig. S3, ESI†). XPS analysis was carried out to investigate the elemental composition of N and C which further provides insightful information regarding the structure of the CzTA-PDAN and CzTA-PDA COPs. The C 1s XPS of the CzTA-PDAN COP showed typical peaks at 281.73 and 282.15 eV attributed to the vinylic C═C and C–C═N units while the peaks at 283.33, 285.38, and 285.88 eV, correspond to the sp^2 C═C of carbazole, C–N of the heteroaromatic carbazole ring, and the cyano carbon in the COP, respectively (Fig. 2a).[62] The N 1s XPS showed typical peaks at 398.55 and 399.95 eV corresponding to the C═N functionality of the cyano group and carbazole C–N, respectively (Fig. 2b). Similarly, C 1s XPS showed typical peaks at 284.68, 286.18, and 287.82 eV, which were attributed to the aromatic sp^2 C═C, imine C═N, and C–N of the carbazole in the COP, respectively. The N 1s XPS showed typical peaks at 399.28 and 400.6 eV, corresponding to the imine C═N functionality and carbazole C–N, respectively (Fig. S4, ESI†). N_2 adsorption–desorption experiments at 77 K were performed to investigate the permanent porosity of the CzTA-PDAN (Fig. 2c) and CzTA-PDA COPs (Fig. S6, ESI†), which showed a type II isotherm which means monolayer–multilayer adsorption of nitrogen on a mesoporous structure of the materials, estimated by nonlocal density functional theory (NLDFT). The Brunauer–Emmett–Teller (BET) surface area was found to be 16.15 $m^2\ g^{-1}$ and

© 2025 The Author(s). Published by the Royal Society of Chemistry

Open Access Article. Published on 11 March 2025. Downloaded on 2/9/2026 11:40:02 PM.
This article is licensed under a Creative Commons Attribution-NonCommercial 3.0 Unported Licence.

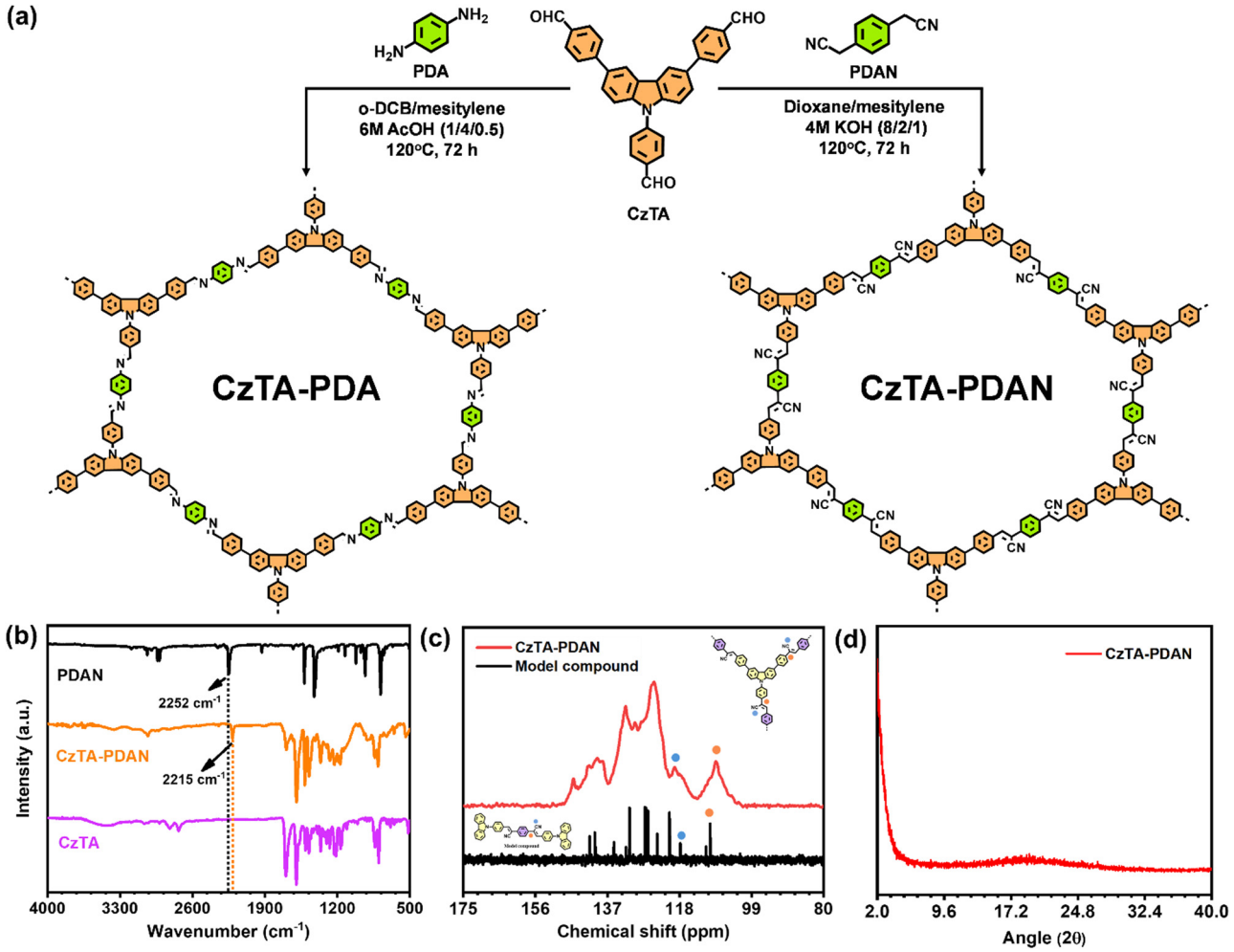

Fig. 1 (a) Synthesis of the CzTA-PDAN COP under solvothermal conditions. (b) FT-IR spectra of the CzTA-PDAN COP. (c) Solid-state ^{13}C CP-MAS NMR spectra of the CzTA-PDAN COP. (d) PXRD pattern of the CzTA-PDAN COP.

11.83 $m^2 g^{-1}$ for CzTA-PDAN and CzTA-PDA COPs, respectively. Furthermore, the thermal stability of the synthesized COPs was determined by thermogravimetric analysis under an N_2 atmosphere, revealing that CzTA-TAPT was stable up to 376 °C (Fig. 2d). SEM images provided visual confirmation of the phase purity, showcasing a distinct nanorod-like morphology for CzTA-PDAN (Fig. 2e) and CzTA-PDA COPs (Fig. S5, ESI†).

The TEM image also shows evidence for a rod-like morphology of the CzTA-PDAN COP (Fig. 2f). The chemical stability of the CzTA-PDAN and CzTA-PDA COPs was examined by immersing the material in 3 M HCl aqueous solution, 3 M NaOH aqueous solution, and various organic solvents for seven days. The CzTA-PDAN COP exhibited excellent stability in all organic solvents as well as under acidic and basic conditions, as indicated by the unchanged FTIR spectrum of the treated CzTA-PDAN COP (Fig. 3a and b). However, the CzTA-PDA COP retained its original structure in organic solvents and 3 M NaOH solution. In contrast, exposure to 3 M HCl solution resulted in a complete structural collapse that is observed by the intensity ratio of imine and aldehyde peaks (Fig. 3c and d). So, FT-IR analyses of the treated Sp^2 C=C linked CzTA-PDAN COP demonstrate excellent chemical stability as compared to the imine-linked CzTA-PDA COP. Ultraviolet-visible diffuse reflectance (UV-DRS) spectra show the absorption maxima at 500 nm for CzTA-PDAN and 450 nm for the CzTA-PDA COP (Fig. 4a). The absorption peaks of the CzTA-PDAN COP exhibit a notable shift towards longer wavelengths compared to the CzTA-PDA COP. This shift arises from the extended conjugation present in the sp^2 carbon-linked COP structure from the carbazole donor to the cyano group acceptor. Furthermore, the optical band gap (Fig. 4b) of CzTA-PDAN measures 2.30 eV, which is narrower compared to that of the CzTA-PDA COP (E_g = 2.53 eV). Mott–Schottky (M–S) measurement was carried out to evaluate the conduction band (CB) position. The M–S plots of CzTA-PDAN and CzTA-PDA display a positive slope, which indicates the n-type semiconductor behavior (Fig. 4c).

It is well known that for the n-type semiconductor, the flat band position is close to the conduction band.[63] Consequently, the conduction band position was calculated to be −1.21 V for CzTA-PDAN and −1.10 V for the CzTA-PDA COP *vs.* SCE. Similarly, the valence band position was further calculated to be 1.09 V and 1.43 V (*vs.* NHE) for CzTA-PDAN and CzTA-PDA,

Open Access Article. Published on 11 March 2025. Downloaded on 2/9/2026 11:40:02 PM.
This article is licensed under a Creative Commons Attribution-NonCommercial 3.0 Unported Licence.

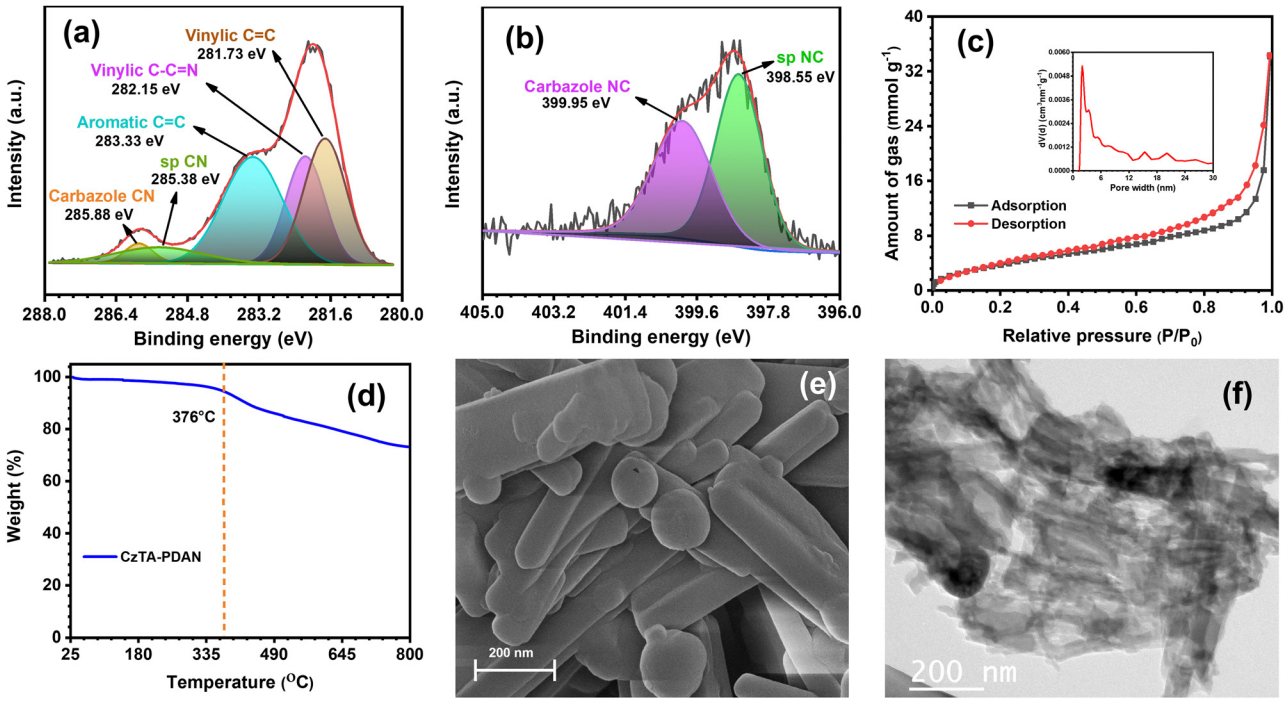

Fig. 2 (a) High-resolution C 1s XPS spectrum and (b) high-resolution N 1s XPS spectrum of the CzTA-PDAN COP. (c) N_2 isotherm of the CzTA-PDAN at 77 K. (d) TGA curve of the CzTA-PDAN COP. (e) FE-SEM image and (d) TEM image of the CzTA-PDAN COP at 200 nm resolution.

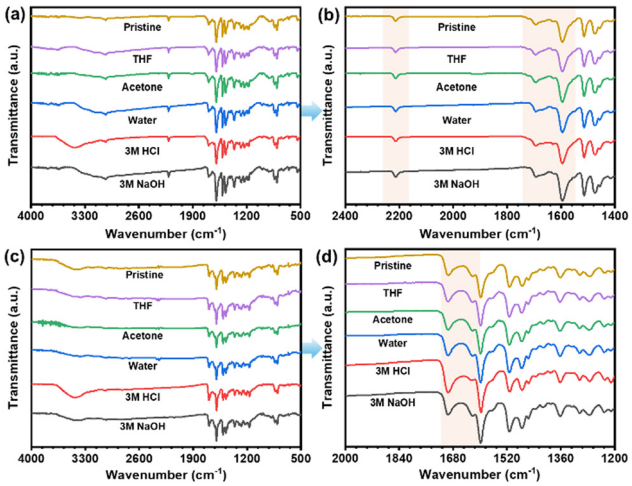

Fig. 3 (a) FT-IR spectra of the CzTA-PDAN COP, (b) expanded FT-IR spectra of the CzTA-PDAN COP, (c) FT-IR spectra of the CzTA-PDA COP, and (d) expanded FT-IR spectra of the CzTA-PDA COP, upon treatment in different organic solvents, 3 M HCl and 3 M NaOH, for 7 days.

respectively. These values were obtained using the equation $E_{CB} = E_{VB} - E_g$, where E_{CB} represents the conduction band edge, E_{VB} represents the valence band edge, and E_g represents the band gap energy. Electrochemical impedance spectroscopy (EIS) was performed to compare the charge transfer resistances (R_{ct}) of the COPs. In the Nyquist plot, the arc radius is smaller for CzTA-PDAN as compared to that for CzTA-PDA, representing the fast photogenerated charge carrier transfer and separation tendency of the sp^2 carbon-linked COP as compared to the imine-linked COP (Fig. 4d).[64] Additionally, the photocurrent densities for the CzTA-PDAN COP as compared to the CzDA-PDA COP suggest more efficient charge separation for the CzTA-PDAN COP (Fig. 4e). The position of conduction and valence bands has been depicted in Fig. 4f for both the COPs.

Photocatalytic degradation of organic dyes

In contrast to CzTA-PDA, the CzTA-PDAN COP exhibits superior charge carrier and separation properties, leading to a significantly higher photocurrent response. This makes CzTA-PDAN a more promising photocatalyst compared to CzTA-PDA. To assess its photocatalytic performance, we conducted dye degradation experiments under visible light irradiation, selecting rhodamine B and Rose Bengal as representative dyes commonly utilized in textile and photo industries. A typical experiment was conducted to study the photodegradation of rhodamine B (RhB) and Rose Bengal (RB) dyes. Initially, 10 mg of catalyst was introduced into a solution containing 50 mL of RhB solution with a concentration of 10^{-5} M. The solution was then left in the dark for 60 minutes to establish adsorption–desorption equilibrium between the photocatalyst and RhB. Subsequently, the solution was exposed to an 18 W white LED light. During the light exposure, samples of 1 mL each of the reaction mixture were extracted at regular time intervals. Following this, the catalyst was separated from the reaction mixture through centrifugation. The concentration of pollutants was determined using a UV-vis spectrophotometer (Shimadzu UV 2600i) by measuring the absorbance at 554 nm within the wavelength

© 2025 The Author(s). Published by the Royal Society of Chemistry

Open Access Article. Published on 11 March 2025. Downloaded on 2/9/2026 11:40:02 PM.
This article is licensed under a Creative Commons Attribution-NonCommercial 3.0 Unported Licence.

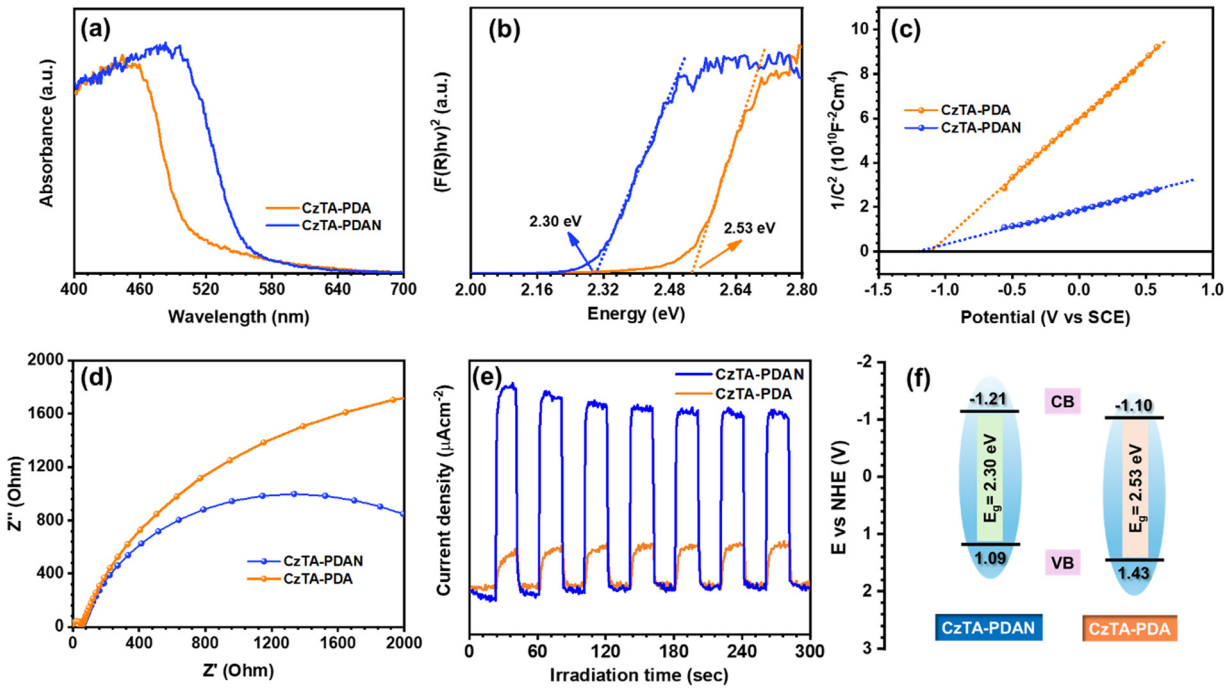

Fig. 4 (a) Solid-state UV-vis diffuse reflectance spectra of the CzTA-PDAN and CzTA-PDA COP. (b)–(g) Tauc plot (b), Mott–Schottky plots (c), electrochemical impedance spectroscopy (EIS) Nyquist plots (d), photocurrent–time plot (e), and band gap energy and band edge positions (f) of the CzTA-PDAN and CzDA-PDA COP.

range of 450–700 nm. After measuring the absorbance at each time interval, the dye solution was returned to the original beaker to ensure a consistent volume of dye solution, thus minimizing errors caused by the potential loss of RhB and catalysts. The photodegradation reaction of RhB was monitored for a duration of up to 80 minutes. Initially, we investigated the impact of pH on the degradation rate of the dye (Section S5.1, ESI†). Our findings revealed that under acidic conditions (pH 2), rhodamine B underwent complete degradation within 80 minutes (Fig. 5a). Following this, we conducted a blank experiment under identical conditions without the CzTA-PDAN COP. The absence of degradation in this control experiment underscores the pivotal role of our catalyst, affirming its significant photocatalytic activity. The photocatalytic degradation proceeded by pseudo-first-order kinetics during the experiments.

To quantify the degradation efficiency in the photodegradation experiments, eqn (1) and (2) were employed.

$$\text{Degradation efficiency (DE)} = C/C_0 \quad (1)$$

$$\text{DE (\%)} = (C/C_0) \times 100 \quad (2)$$

The kinetics of the photocatalytic rhodamine B degradation were investigated based on the Langmuir–Hinshelwood model.

$$\ln(C/C_0) = kt \quad (3)$$

where C_0 is the initial concentration of the dye, C is the remaining concentration of the dye at time t, and k is the pseudo-first-order rate constant.

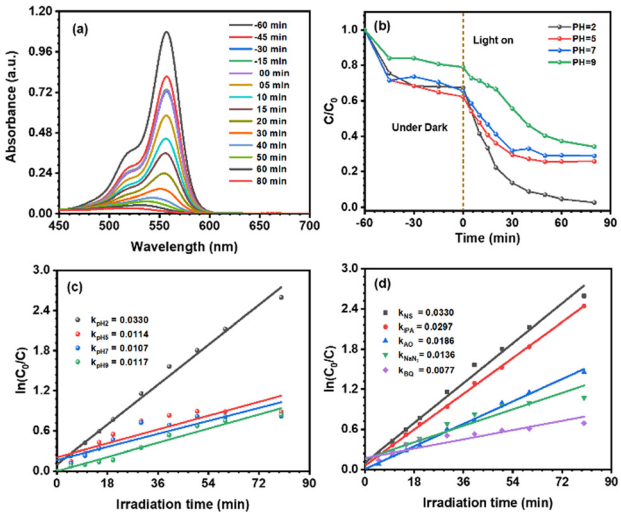

Fig. 5 (a) Photocatalytic degradation of RhB at pH 2 under the irradiation of an 18 W white CFL catalyzed by the CzTA-PDAN COP. (b) Impact of pH on the degradation of dye. (c) Primary photodegradation rate of RhB at different pH values. (d) Primary photodegradation rate in the presence of a scavenger.

As shown in Fig. 5b and c the degradation efficiency of the catalyst was decreasing with the increasing pH of the dye solution. So, the CzTA-PDAN catalyst shows effective RhB photodegradation at pH 2. Additionally, we performed the degradation study for Rose Bengal (RB) dye at a neutral pH 7

Open Access Article. Published on 11 March 2025. Downloaded on 2/9/2026 11:40:02 PM.
This article is licensed under a Creative Commons Attribution-NonCommercial 3.0 Unported Licence.

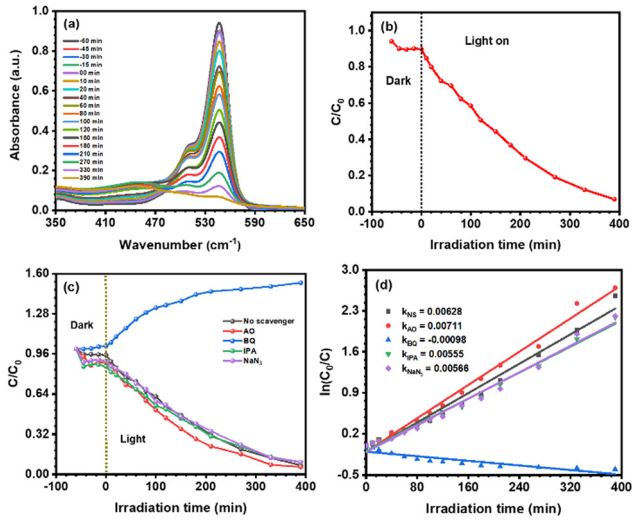

Fig. 6 (a) Photocatalytic degradation of RB at pH 7 under the irradiation of an 18 W white CFL catalyzed by the CzTA-PDAN COP. (b) Photodegradation rate of RB at (pH = 7) under the irradiation of an 18 W white CFL. (c) Photodegradation rate of RB in the presence of a scavenger. (d) Primary photodegradation rate in the presence of a scavenger.

(Fig. 6a and b). In this case, the complete degradation was observed in 380 minutes under the irradiation of an 18 W white LED light with catalyst loading 0.2 g L^{-1}.

Photocatalytic degradation of rhodamine B (RhB) under sunlight

To see the effectiveness of our CzTA-PDAN COP, we have performed the RhB dye degradation experiment in the presence of sunlight. As shown in the figure the degradation rate in the presence of sunlight is higher than the white light-irradiated dye degradation (Fig. 7a and b). So, this result proves the greener approach of our catalyst CzTA-PDAN for the degradation of dyes and has proven the practical application of the catalyst.

Photodegradation pathway of dyes

The degraded samples of both pollutants, RhB and RB, subjected to visible light irradiation with the CzTA-PDAN COP as the photocatalyst, were analysed using mass spectrometry to identify degradation fragments. Reaction mixtures collected at different time intervals were examined, revealing the high degradation efficiency of the CzTA-PDAN COP for RhB and RB dyes. High-resolution mass spectrometry (HRMS) was employed to investigate the key degradation intermediates at various stages. The analysis results, including HRMS spectra (Fig. S21 and S22, ESI†) and major detected intermediates (Tables S1 and S2, ESI†), confirmed the breakdown of both dyes into low-molecular-weight compounds. Based on these findings and relevant literature, the potential photodegradation pathways of the dyes are proposed in Schemes S5 and S6 (ESI†).[65,66] As per existing research, initially, the photocatalyst targets bonds with lower energy, including C–C and C–N bonds, initiating degradation. For instance, in the degradation process of dyes like RhB and RB, an *N*-dealkylation pathway alongside some C–C bond breakage compromises the structural integrity of the dyes, disrupting the overall electron conjugation. Consequently, noticeable blue shifts in the λ_{max} of the dyes are observed during the photocatalytic process. Subsequently, bonds possessing higher energy, such as –C–S–, –C–N–, and –C–C– bonds within chromophore groups, and –N=N– bonds, undergo photodegradation. This aligns with the disappearance of all absorption bands in the UV spectra throughout degradation. Eventually, the dyes degrade into smaller aromatic groups and various low molecular weight compounds.

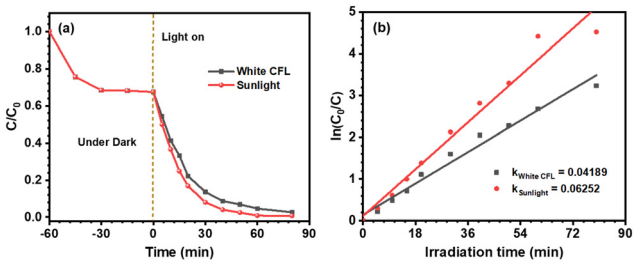

Fig. 7 (a) Photocatalytic degradation of RhB at pH 2 under the irradiation of an 18 W white CFL (black) as well as sunlight (red) catalyzed by the CzTA-PDAN COP. (b) Primary photodegradation rate of RhB at pH 2 under the irradiation of an 18 W white CFL (black) as well as sunlight (red).

Mechanism study for photocatalytic dye degradation

As we know the photocatalytic degradation of dyes involves the reactive oxygen species (ROS) and holes.[67] There are three ROS which are the superoxide radical anion, singlet oxygen and hydroxy radical. So, to gain deeper insights into the photocatalytic mechanism and the functions of active species, we utilized an indirect chemical probe approach employing scavengers like benzoquinone (BQ), sodium azide (NaN_3), isopropyl alcohol (IPA), and ammonium oxalate (AO). These scavengers were selected to specifically target and investigate the roles of the superoxide radical anion ($^{\bullet}O_2^-$), singlet oxygen ($^1O_2$), hydroxyl radical ($^{\bullet}OH$), and the positively charged holes (h^+) in the process.[68] The introduction of substances like BQ, AO, and NaN_3 resulted in a reduction in the degradation efficiency in the case of RhB. However, when IPA was added, there was minimal observable difference (Fig. 5d). This suggests that the photocatalytic degradation process is primarily influenced by the superoxide radical anion, singlet oxygen, and holes. Notably, hydroxy radicals appear to play no significant role in this process.

Similarly, in the case of Rose Bengal, the photocatalytic activity is drastically suppressed in a controlled experiment when BQ is used as a superoxide radical anion scavenger. However, no significant change in the degradation of rose Bengal is observed upon the addition of AO, IPA, and NaN_3 as h^+, $^{\bullet}OH$, and $^1O_2$ scavengers under similar conditions (Fig. 6d). This indicates that the superoxide radical anion ($^{\bullet}O_2^-$) is the only responsible active species for the degradation of rose Bengal under visible light. After confirming the role of reactive species, a reasonable photocatalytic mechanism of

© 2025 The Author(s). Published by the Royal Society of Chemistry

Open Access Article. Published on 11 March 2025. Downloaded on 2/9/2026 11:40:02 PM.
This article is licensed under a Creative Commons Attribution-NonCommercial 3.0 Unported Licence.

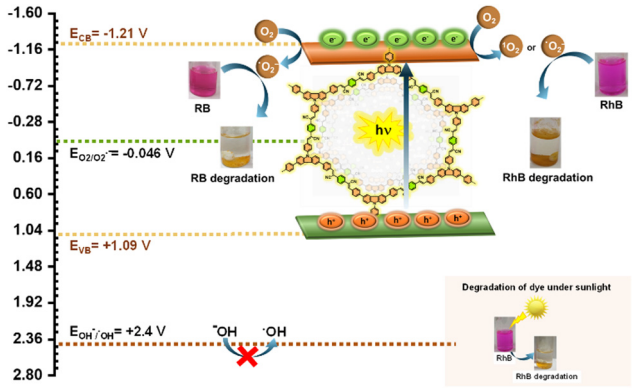

Fig. 8 The possible mechanisms of photocatalytic degradation of organic dyes catalyzed by the CzTA-PDAN COP.

organic dye degradation was summarized by the band structure (Fig. 8). The conduction band position of the CzTA-PDAN COP was calculated as −1.21 V. The determination of bandgap energies (E_g) is facilitated through the analysis of UV-visible spectra employing the Kubelka–Munk equation and the calculated bandgap energies (E_g) for CzTA-PDAN was found to be 2.30 eV. The E_{CB} potential is more negative than the reduction potential required for molecular oxygen to superoxide radical conversion, indicating that CzTA-PDAN could produce $^{\bullet}O_2^-$. The E_{VB} potentials of CzTA-PDAN were measured at +1.09 V, which is lower than the oxidation potential of $OH^-/^{\bullet}OH$ at +2.40 eV. This contrast strongly suggests the limited production of $^{\bullet}OH$ during photocatalysis. These analyses were supported by the scavenger study also. So, in the photocatalytic dye degradation upon irradiation with visible light the catalyst will generate the hole and electron pairs. The excited electrons in the conduction band will interact with the molecular oxygen to produce the superoxide radical anion and singlet oxygen and finally, both reactive oxygen species interact with the organic dye, causing the degradation of the dye. Additionally, the π–π interaction of the dye molecule with the highly conjugated CzTA-PDAN COP accelerates the diffusion of dyes to the active site of the catalyst and promotes degradation.

Recyclability test

To demonstrate the chemical stability and heterogeneous catalytic efficiency, we performed the experiment for up to five cycles under identical conditions. Remarkably, no decrease in catalytic efficiency was observed for dye degradation throughout these cycles (Fig. 9a). Subsequent FT-IR analysis of the recycled COP revealed no change in peak intensity and position, confirming the structural integrity of the CzTA-PDAN COP even after five cycles (Fig. 9b). These findings underscore the exceptional recyclability and stability demonstrated by the materials.

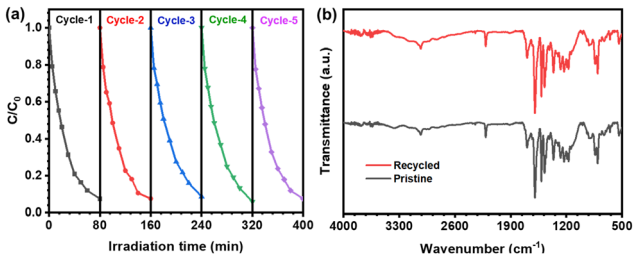

Fig. 9 (a) Recyclability test of the CzTA-PDAN COP for the photocatalytic removal of RhB. (b) FT-IR spectra of the recycled CzTA-PDAN COP.

Conclusions

In summary, carbazole-based sp^2 carbon-linked CzTA-PDAN and imine-linked CzTA-PDA COPs were successfully synthesized under solvothermal conditions. Both the COPs have the same monomer but a different linkage. Because of the extended conjugation, the CzTA-PDAN COP demonstrated enhanced charge separation, and a higher photocurrent response compared to the CzTA-PDA COP. Additionally, due to its outstanding photocatalytic activity, the sp^2c-COP was employed for the photocatalytic degradation of RhB and RB under an 18 W white CFL. We explored the degradation of RhB under sunlight, and more than 99% degradation was observed within 60 minutes, which demonstrates the practical applicability of our catalyst. From the mechanistic point of view, the superoxide radical anion, singlet oxygen, and holes are the active species responsible for dye degradation. Moreover, CzTA-PDAN shows good reusability up to five cycles without the loss of photocatalytic activity. So, this work provides a greener approach for wastewater treatment and opens up a new path to develop new metal-free catalysts and utilize solar energy for other sustainable uses.

Author contributions

K. V.: conceptualization, methodology, validation, formal analysis, data curation, writing – original draft and visualization. K. R. J. T.: conceptualization, review and editing, supervision, funding acquisition. All authors have given approval to the final version of the manuscript.

Data availability

The data supporting this article have been included as part of the ESI.†

Conflicts of interest

There are no conflicts to declare.

Acknowledgements

We gratefully acknowledge the financial support from the Science and Engineering Research Board (SERB), New Delhi (CRG/2022/001770). Kamal Verma is grateful to University Grant Commission (UGC), Government of India, for research fellowship.

Open Access Article. Published on 11 March 2025. Downloaded on 2/9/2026 11:40:02 PM.
This article is licensed under a Creative Commons Attribution-NonCommercial 3.0 Unported Licence.

References

1 W. Dorigo, S. Dietrich, F. Aires, L. Brocca, S. Carter, J. F. Cretaux, D. Dunkerley, H. Enomoto, R. Forsberg, A. Güntner and M. I. Hegglin, *Bull. Am. Meteorol. Soc.*, 2021, **102**, E1897–E1935.
2 R. Al-Tohamy, S. S. Ali, F. Li, K. M. Okasha, Y. A. G. Mahmoud, T. Elsamahy, H. Jiao, Y. Fu and J. Sun, *Ecotoxicol. Environ. Saf.*, 2022, **231**, 113160.
3 S. Kamino and M. Uchiyama, *Org. Biomol. Chem.*, 2023, **21**, 2458–2471.
4 A. Jakimińska, M. Pawlicki and W. Macyk, *J. Photochem. Photobiol., A*, 2022, **433**, 114176.
5 J. Kaur and S. Singhal, *Phys. Rev. B: Condens. Matter*, 2014, **450**, 49–53.
6 M. M. Mabel, T. R. Sundararaman, N. Parthasarathy and J. Rajkumar, *J. Environ. Biol.*, 2019, **40**, 349–355.
7 C. Zubieta, M. B. Sierra, M. A. Morini, P. C. Schulz, L. Albertengo and M. S. Rodríguez, *Colloid Polym. Sci.*, 2008, **286**, 377–384.
8 A. K. Al-Buriahi, A. A. Al-Gheethi, P. S. Kumar, R. M. S. R. Mohamed, H. Yusof, A. F. Alshalif and N. A. Khalifa, *Chemosphere*, 2022, **287**, 132162.
9 N. Yadav, S. Payra, P. Tamuly and J. N. Moorthy, *Org. Biomol. Chem.*, 2023, **21**, 7994–8002.
10 Z. Y. Yu, J. N. Zhao, F. Yang, X. F. Tang, Y. F. Wu, C. F. Ma, B. Song, L. Yun and Q. W. Meng, *RSC Adv.*, 2020, **10**, 4825–4831.
11 F. K. C. Leung, J. F. Cui, T. W. Hui, K. K. Y. Kung and M. K. Wong, *Asian J. Org. Chem.*, 2015, **4**, 533–536.
12 D. P. Patel and S. Kumar Singh, *Eur. J. Org. Chem.*, 2024, e202301185.
13 E. Colombo, M. Fiorenza Boselli, L. Raimondi, A. Puglisi and S. Rossi, *Helv. Chim. Acta*, 2023, **106**, e202300132.
14 K. Melaniuk, *Front. Mar. Sci.*, 2021, **8**, 587748.
15 X. W. Yu, X. Liu, Y. W. Jiang, Y. H. Li, G. Gao, Y. X. Zhu, F. Lin and F. G. Wu, *Anal. Chem.*, 2022, **94**, 4243–4251.
16 A. D. Smith McWilliams, S. Ergülen, M. M. Ogle, C. A. de Los Reyes and M. Pasquali, *Pure Appl. Chem.*, 2020, **92**, 265–274.
17 H. S. Lv, S. Y. Huang, B. X. Zhao and J. Y. Miao, *Anal. Chim. Acta*, 2013, **788**, 177–182.
18 R. Al-Tohamy, S. S. Ali, F. Li, K. M. Okasha, Y. A. G. Mahmoud, T. Elsamahy, H. Jiao, Y. Fu and J. Sun, *Ecotoxicol. Environ. Saf.*, 2022, **231**, 113160.
19 C. V. Nachiyar, A. D. Rakshi, S. Sandhya, N. B. D. Jebasta and J. Nellore, *Chem. Environ. Eng.*, 2023, 100339.
20 M. Shabil Sha, H. Anwar, F. N. Musthafa, H. Al-Lohedan, S. Alfarwati, J. R. Rajabathar, J. J. Khalid Alahmad, J. J. Cabibihan, M. Karnan and K. Kumar Sadasivuni, *Sci. Rep.*, 2024, **14**, 3608.
21 G. Gogoi, S. Saikia, A. Das, S. Saikia, N. Hoque, S. Biswas, M. Dey, P. K. Kalita and K. K. Bania, *Chem. Sel.*, 2023, **8**, e202300279.
22 O. Mapazi, P. Matabola, T. Mokhena and H. van Der Walt, *J. Appl. Polym. Sci.*, 2023, **140**, e53679.
23 H. M. Abo-Dief, O. K. Hussein, A. Ihsan, S. M. El-Bahy, A. M. Raslan, M. Shahid and M. F. Warsi, *Ceram. Int.*, 2022, **48**, 22228–22236.
24 P. Muthukumar, D. Yuvapriya, D. Selvakumar, S. N. Sri, N. Saisubramanian, M. Pannipara, A. G. Al-Sehemi and S. P. Anthony, *Mater. Sci. Eng. B*, 2023, **296**, 116688.
25 G. H. Matar and M. Andac, *Inorg. Chem. Commun.*, 2023, **153**, 110889.
26 N. Karousis and D. Tasis, *Energy Adv.*, 2024, **3**, 712–740.
27 N. Xu, Y. Diao, Z. Xu, H. Ke and X. Zhu, *ACS Appl. Energy Mater.*, 2022, **5**, 7473–7478.
28 H. Wang, L. Shi, Z. Qu, L. Zhang, X. Wang, Y. Wang, S. Liu, H. Ma and Z. Guo, *ACS Appl. Mater. Interfaces*, 2024, **16**, 2296–2308.
29 M. C. Borrallo-Aniceto, M. Pintado-Sierra, A. Valverde-González, U. Díaz, E. M. Maya and M. Iglesias, *Green Chem.*, 2024, **26**, 1975–1983.
30 H. Chen, A. M. Gardner, G. Lin, W. Zhao, M. Bahri, N. D. Browning, R. S. Sprick, X. Li, X. Xu and A. I. Cooper, *Catal. Sci. Technol.*, 2022, **12**, 5442–5452.
31 Z. Wang, X. Yang, T. Yang, Y. Zhao, F. Wang, Y. Chen, J. H. Zeng, C. Yan, F. Huang and J. X. Jiang, *ACS Catal.*, 2018, **8**, 8590–8596.
32 C. Han, S. Xiang, S. Jin, C. Zhang and J. X. Jiang, *ACS Catal.*, 2022, **13**, 204–212.
33 J. Zang, C. Bao, H. Li, Y. Gao, X. Dou, Y. Li, W. Dong, L. Shi, Y. Li and Q. Duan, *New J. Chem.*, 2024, **48**, 8472–8478.
34 S. Gan, Y. Zeng, C. Lu, M. Ma, F. Wang, G. Yang, Y. Zhang and J. Nie, *Catal. Sci. Technol.*, 2022, **12**, 6548–6555.
35 N. Yin, W. Chen, Y. Yang, Z. Tang, P. Li, X. Zhang, L. Tang, T. Wang, Y. Wang and Y. Zhou, *Chin. J. Catal.*, 2023, **51**, 168–179.
36 H. Xu, Y. Xu, Y. Wang, Q. Wang, M. W. Wong and L. Yu, *Org. Chem. Front.*, 2023, **10**, 1050–1061.
37 K. S. Novoselov, D. Jiang, F. Schedin, T. J. Booth, V. V. Khotkevich, S. V. Morozov and A. K. Geim, *Proc. Natl. Acad. Sci. U. S. A.*, 2005, **102**, 10451–10453.
38 M. Wang, S. Fu, P. Petkov, Y. Fu, Z. Zhang, Y. Liu, J. Ma, G. Chen, S. M. Gali, L. Gao and Y. Lu, *Nat. Mater.*, 2023, **22**, 880–887.
39 X. Liang, Z. Ni, L. Zhao, B. Ge, H. Zhao and W. Li, *Mater. Chem. Phys.*, 2021, **270**, 124725.
40 E. Dautzenberg, M. Lam, G. Li and L. C. de Smet, *Nanoscale*, 2021, **13**, 19446–19452.
41 R. Shevate and D. L. Shaffer, *ACS Nano*, 2022, **16**, 2407–2418.
42 Z. Meng and K. A. Mirica, *Chem. Soc. Rev.*, 2021, **50**, 13498–13558.
43 S. Biswas, A. Dey, F. A. Rahimi, S. Barman and T. K. Maji, *ACS Catal.*, 2023, **13**, 5926–5937.
44 Y. Kumar, I. Ahmad, A. Rawat, R. K. Pandey, P. Mohanty and R. Pandey, *ACS Appl. Mater. Interfaces*, 2024, **16**, 11605–11616.
45 L. Deng, X. Kang, T. Quan, L. Yang, S. Liu, K. Zhang, M. Gao, Z. Xia and D. Gao, *ACS Appl. Mater. Interfaces*, 2021, **13**, 33449–33463.
46 M. Afshari, M. Dinari, H. Farrokhpour and F. Zamora, *ACS Appl. Mater. Interfaces*, 2022, **14**, 22398–22406.

© 2025 The Author(s). Published by the Royal Society of Chemistry

Open Access Article. Published on 11 March 2025. Downloaded on 2/9/2026 11:40:02 PM.
This article is licensed under a Creative Commons Attribution-NonCommercial 3.0 Unported Licence.

47 W. Huang, W. Zhang, S. Yang, L. Wang and G. Yu, *Small*, 2024, **20**, 2308019.
48 C. Wu, X. Li, M. Shao, J. Kan, G. Wang, Y. Geng and Y. B. Dong, *Chin. Chem. Lett.*, 2022, **33**, 4559–4562.
49 F. Zhang, Y. Wang, H. Zhao, X. Dong, X. K. Gu and X. Lang, *ACS Appl. Mater. Interfaces*, 2024, **16**, 8772–8782.
50 D. Chen, W. Chen, G. Zhang, S. Li, W. Chen, G. Xing and L. Chen, *ACS Catal.*, 2021, **12**, 616–623.
51 F. Yang, C. C. Li, C. C. Xu, J. L. Kan, B. Tian, H. Y. Qu, Y. Guo, Y. Geng and Y. B. Dong, *Chem. Commun.*, 2022, **58**, 1530–1533.
52 K. Verma, M. A. Addicoat and K. R. Justin Thomas, *ACS Appl. Polym. Mater.*, 2024, **6**, 3909–3917.
53 A. Acharjya, P. Pachfule, J. Roeser, F. J. Schmitt and A. Thomas, *Angew. Chem., Int. Ed.*, 2019, **58**, 14865–14870.
54 W. Wang, K. Cai, W. Zhou, F. Tao, Z. Li, Q. Lin, L. Wang, Z. Yu, J. Zhang and H. Zhou, *ACS Appl. Nano Mater.*, 2023, **6**, 8396–8403.
55 H. Ji, G. Yan, P. Zou, H. Wang, M. Li, Y. Feng, X. Qu, D. Geng and X. Zhang, *Chem. – Eur. J.*, 2023, **29**, e202202787.
56 J. Xu, C. Yang, S. Bi, W. Wang, Y. He, D. Wu, Q. Liang, X. Wang and F. Zhang, *Angew. Chem.*, 2020, **132**, 24053–24061.
57 S. Xu, Z. Liao, A. Dianat, S. W. Park, M. A. Addicoat, Y. Fu, D. L. Pastoetter, F. G. Fabozzi, Y. Liu, G. Cuniberti and M. Richter, *Angew. Chem.*, 2022, **134**, e202202492.
58 D. L. Pastoetter, S. Xu, M. Borrelli, M. Addicoat, B. P. Biswal, S. Paasch, A. Dianat, H. Thomas, R. Berger, S. Reineke and E. Brunner, *Angew. Chem., Int. Ed.*, 2020, **59**, 23620–23625.
59 K. Lei, D. Wang, L. Ye, M. Kou, Y. Deng, Z. Ma, L. Wang and Y. Kong, *ChemSusChem*, 2020, **13**, 1725–1729.
60 H. He, X. Fang, D. Zhai, W. Zhou, Y. Li, W. Zhao, C. Liu, Z. Li and W. Deng, *Chem. – Eur. J.*, 2021, **27**, 14390–14395.
61 A. F. El-Mahdy, A. M. Elewa, S. W. Huang, H. H. Chou and S. W. Kuo, *Adv. Opt. Mater.*, 2020, **8**, 2000641.
62 X. Zhuang, W. Zhao, F. Zhang, Y. Cao, F. Liu, S. Bi and X. Feng, *Polym. Chem.*, 2016, **7**, 4176–4181.
63 L. Niu, J. Du, D. Jiang, H. Du, X. Lin, J. Xu, Z. Li, C. Zhu, L. Gu, H. Bi and Y. Yuan, *Catal. Lett.*, 2022, **152**, 669–678.
64 X. Shan, G. Ge and Z. Zhao, *ChemCatChem*, 2019, **11**, 1534–1544.
65 M. Sharma, R. Singh, A. Sharma and V. Krishnan, *Dalton Trans.*, 2024, **53**, 6731–6746.
66 Y. Du, H. Ai, Y. Liu and H. Liu, *Sustainable Energy Fuels*, 2023, **7**, 1747–1754.
67 T. Xia, Z. Wu, Y. Liang, W. Wang, Y. Li, Z. Sui, L. Shan, C. Li, R. Fan and Q. Chen, *Mater. Today Chem.*, 2022, **25**, 100962.
68 Y. Park, Y. Na, D. Pradhan, B. K. Min and Y. Sohn, *CrystEngComm*, 2014, **16**, 3155–3167.

© 2025 The Author(s). Published by the Royal Society of Chemistry